

Optical inverse-Compton emission from clusters of galaxies

Ryo Yamazaki^{1,2*} and Abraham Loeb²

¹*Department of Physics and Mathematics, Aoyama Gakuin University, 5-10-1, Fuchinobe, Sagami-hara 252-5258, Japan*

²*Harvard-Smithsonian Center for Astrophysics, 60 Garden Street, Cambridge, MA, 02138, USA*

12 August 2015

ABSTRACT

Shocks around clusters of galaxies accelerate electrons which upscatter the Cosmic Microwave Background photons to higher-energies. We use an analytical model to calculate this inverse Compton (IC) emission, taking into account the effects of additional energy losses via synchrotron and Coulomb scattering. We find that the surface brightness of the optical IC emission increases with redshift and halo mass. The IC emission surface brightness, 32–34 mag arcsec^{−2}, for massive clusters is potentially detectable by the newly developed Dragonfly Telephoto Array.

Key words: acceleration of particles — galaxies: clusters: general — intergalactic medium — radiation mechanisms: nonthermal

1 INTRODUCTION

According to the standard model of hierarchical structure formation, accretion shocks occur around the virial radii of massive clusters (e.g., Ryu et al. 2003; Schaal & Springel 2015, and references therein). In these shocks, electrons are expected to be accelerated by first-order Fermi mechanism (see, e.g., Brunetti & Jones 2014, for recent review) to have power-law distribution (Blandford & Ostriker 1978; Bell 1978). Turbulence in the intergalactic medium (IGM; Ryu et al. 2008; Takizawa 2008; Miniati 2015) is another source of particle acceleration via second-order Fermi mechanism (Schlickeiser et al. 1987; Brunetti et al. 2001; Petrosian 2001; Fujita et al. 2003). Relativistic electrons give rise to inverse Compton (IC) emission by upscattering Cosmic Microwave Background (CMB) photons as well as radio synchrotron emission. So far, IC emission has been studied mainly in hard X-ray and gamma-ray bands both theoretically and observationally (Sarazin 1999; Loeb & Waxman 2000; Totani & Kitayama 2000; Takizawa & Naito 2000; Fujita & Sarazin 2001; Takizawa 2002; Keshet et al. 2003, 2004a, 2012; Petrosian et al. 2008; Kushnir & Waxman 2010; Bartels et al. 2015). However, currently there are only upper limits (Ota et al. 2014; Gastaldello et al. 2015, and references therein) and a few claimed detections of hard X-rays (Rephaeli et al. 2008), but no detection in the gamma-ray band (Ackermann et al. 2010, 2014), which may constrain particle acceleration mechanisms (e.g., Zandanel & Ando 2014; Vazza et al. 2015). Although IC emission from individual clusters has not yet

been detected, the cumulative emission from all of them may contribute to extragalactic gamma-ray background (Loeb & Waxman 2000; Miniati 2002).

In this paper, we focus on the IC emission namely in the optical band. So far, it has been thought that the optical IC emission is too dim to be detectable (e.g., Sarazin 1999; Fujita & Sarazin 2001). However, an advanced technique has recently been developed in the form of the Dragonfly Telephoto Array (Abraham & van Dokkum 2014; van Dokkum et al. 2014), which is optimized for the detection of extended ultra low surface brightness structures and is capable of imaging extended structures to surface brightness levels below 32 mag arcsec^{−2} in the SDSS g band with a reasonable exposure time. This newly developed technique provides a new motivation for calculating the brightness of the optical IC emission in detail. Since no firm detection of IC emission at any wavelength has been reported as of yet, the optical telescopes hold the potential to bring the first clear detection of the IC emission from large-scale shocks around clusters of galaxies, which is also the first evidence of nonthermal processes at accretion shocks.

We construct a simple one zone, analytical model for IC emission from cluster shocks, allowing us to capture the essential physical details as well as the parameter dependence of the results. Because the electrons emitting the optical IC emission have the Lorentz factor ~ 50 , they are potentially affected by Coulomb energy losses (e.g., Sarazin 1999; Petrosian et al. 2008). However, as we show later, this effect is not significant. Our model applies also to other sources of nonthermal electrons. We focus on IC from primarily accelerated electrons for simplicity, although secondary electrons may also contribute (e.g., Blasi & Colafrancesco 1999;

* E-mail: ryo@phys.aoyama.ac.jp

Miniati 2003; Inoue et al. 2005; Kushnir & Waxman 2009). For the small magnetic field strength expected in clusters, the contribution of synchrotron emission to the optical brightness is negligible.

Our paper is organized as follows. In section 2, we describe our analytical model for calculating the IC emission. The surface brightness in the SDSS g-band is then calculated for fiducial parameters in section 3. Finally, we summarize our results and predictions for specific clusters in section 4. Throughout the paper, we assume a flat Λ CDM universe with cosmological parameters, $h = 0.6774$, $\Omega_m = 0.3089$, $\Omega_\Lambda = 0.6911$, and $\Omega_b = 0.0486$ (Ade et al. 2015)

2 ANALYTICAL MODEL OF IC SPECTRUM

2.1 Physical quantities of cluster shocks

A halo of mass M collapsing at redshift z has a virial radius r_{vir} , within which the mean density is Δ_c times the critical density $\rho_c(z)$, and circular velocity at the virial radius V_c given by (Bryan & Norman 1998; Barkana & Loeb 2001),

$$\begin{aligned} r_{\text{vir}} &= \left(\frac{3M}{4\pi\Delta_c\rho_c(z)} \right)^{1/3} \\ &= 0.79 h^{-2/3} M_{14}^{1/3} w(z)^{-1/3} (1+z)^{-1} \text{Mpc} , \end{aligned} \quad (1)$$

$$\begin{aligned} V_c &= \sqrt{\frac{GM}{r_{\text{vir}}}} \\ &= 7.4 \times 10^7 h^{1/3} M_{14}^{1/3} w(z)^{1/6} (1+z)^{1/2} \text{cm s}^{-1} , \end{aligned} \quad (2)$$

where $M_{14} = (M/10^{14} M_\odot)$. The function $w(z)$ is given by

$$w(z) = \frac{\Omega_m}{\Omega_m^z} \frac{\Delta_c}{18\pi^2} , \quad (3)$$

where

$$\Omega_m^z = \frac{\Omega_m(1+z)^3}{\Omega_m(1+z)^3 + \Omega_\Lambda} , \quad (4)$$

$$\Delta_c = 18\pi^2 + 82(\Omega_m^z - 1) - 39(\Omega_m^z - 1)^2 . \quad (5)$$

Note that $w(z)$ is a monotonically decreasing function of z , starting at $w(0) = 0.58$, decaying through $w(1) = 0.35$ and asymptotically approaching $w(z) \rightarrow \Omega_m = 0.31$ as $z \rightarrow \infty$.

For simplicity, we assume that a spherical virial shock is formed at r_{vir} , and that accretion is smooth and not associated with mergers of sub-units. Recent numerical simulations have shown that accretion shocks are deformed and far from spherical (e.g., Ryu et al. 2003; Lau et al. 2015; Schaal & Springel 2015; Nelson et al. 2015), however, ensemble-averaged gas profile shows that virial shocks exist near the virial radius. Future extensions of this work can be based on numerical simulations of non-spherical configurations. The ensemble-averaged mass accretion rate onto the halo is written as (White 1994),

$$\dot{M} = f_{\text{acc}} \frac{V_c^3}{G} , \quad (6)$$

and the shock temperature is given by,

$$kT = f_T \mu m_p V_c^2 , \quad (7)$$

where μm_p is the average mass of a particle (including electrons), and we adopt $\mu = 0.6$. The factors f_{acc} and f_T are

dimensionless numbers of order unity. The gas density just in front of the shock can be written as,

$$\begin{aligned} n_g &= \frac{(\Omega_b/\Omega_m)\dot{M}}{4\pi r_{\text{vir}}^2 V_c \mu m_p} \\ &= 8.0 \times 10^{-5} f_{\text{acc}} w(z) (1+z)^3 \text{cm}^{-3} . \end{aligned} \quad (8)$$

This estimate is roughly consistent with the results given by Patej & Loeb (2015) if $f_{\text{acc}} \approx 0.5$. The gas is compressed at the shock with shock compression ratio r , which is somewhat uncertain. Recent numerical simulations have shown that the shocks are not so strong and their typical Mach number is around a few (Ryu et al. 2003; Schaal & Springel 2015), i.e., $r < 4$. The IGM is pre-heated and the shocks are not so strong at present epoch $z \sim 0$, however, at high redshifts $z \gtrsim 1$ when the IGM is cold, the shocks around clusters are likely to be strong ($r \approx 4$). Fortunately, we will see in section 3 that the IC flux does not depend on r for fiducial parameters.

The magnetic field around the shock is amplified as in supernova remnants (e.g., Vink & Laming 2003; Bamba et al. 2003, 2005a,b). Assuming that the energy density of the downstream magnetic field constitutes a fraction ξ_B of the downstream thermal energy density, we estimate the magnetic field strength as (Waxman & Loeb 2000; Keshet et al. 2004b; Fujita & Kato 2005; Kushnir & Waxman 2009),

$$\begin{aligned} B &= (12\pi r \xi_B n_g f_T \mu m_p)^{1/2} V_c \\ &= 0.72 (r_4 f_T f_{\text{acc}} \xi_{B,-2})^{1/2} M_{14}^{1/3} w(z)^{2/3} (1+z)^2 \mu\text{G} \end{aligned} \quad (9)$$

where $\xi_{B,-2} = (\xi_B/0.01)$ and $r_4 = (r/4)$.

2.2 Injected electron spectrum

We assume a single power-law form of injected electrons

$$\dot{N}(\gamma) = N_0 \gamma^{-p} , \quad (\gamma_{\text{min}} < \gamma < \gamma_{\text{max}}) , \quad (10)$$

with a constant normalization N_0 and a spectral index p .

The maximum Lorentz factor, γ_{max} , is determined by the balance of acceleration time and the cooling time. The acceleration time is given by (Drury 1983),

$$t_{\text{acc}}(\gamma) = \frac{r(r+1)}{r-1} \frac{\eta_g \gamma m_e c^3}{e B v_{\text{sh}}^2} , \quad (11)$$

where the gyro-factor η_g is of order unity, and the shock velocity that is measured in the rest frame of the shock, v_{sh} , is related to V_c through $v_{\text{sh}} = [r/(r-1)]V_c$. Here we assume Bohm diffusion with no change in the diffusion properties across the shock, and no shock modification due to accelerated particles. We equate t_{acc} to the cooling time via synchrotron and IC emission,

$$t_{\text{IC/syn}}(\gamma) = \frac{6\pi m_e c}{\sigma_T (B^2 + B_{\text{CMB}}^2) \gamma} , \quad (12)$$

where $B_{\text{CMB}} = 3.24 (1+z)^2 \mu\text{G}$, to obtain (Loeb & Waxman 2000),

$$\begin{aligned} \gamma_{\text{max}} &= 3.4 \times 10^7 r_4^{3/4} \left(\frac{15}{r^2 - 1} \right)^{1/2} \\ &\times \frac{(f_T f_{\text{acc}} \xi_{B,-2})^{1/4} M_{14}^{1/2} w(z)^{1/2}}{\eta_g^{1/2} [1 + (B/B_{\text{CMB}})^2]^{1/2} (1+z)^{1/2}} , \end{aligned} \quad (13)$$

based on Eqs. (2) and (9). We note that the effect of synchrotron cooling is negligible since,

$$\left(\frac{B}{B_{\text{CMB}}}\right)^2 = 4.9 \times 10^{-2} r_4 f_{\text{T}} f_{\text{acc}} \xi_{\text{B},-2} M_{14}^{2/3} w(z)^{4/3} \quad , \quad (14)$$

is always small for our adopted parameters.

In order to determine both the normalization constant N_0 and the minimum Lorentz factor γ_{min} , we make two assumptions. One is that the production rate of the accelerated electrons is a fraction η_e of the particle number input rate across the virial shock, $\dot{N}_{\text{in}} = (\Omega_{\text{b}}/\Omega_{\text{m}})\dot{M}/\mu m_p$. The other is that a fraction ξ_e of thermal shock energy $(3/2)kT\dot{N}_{\text{in}}$ is carried by relativistic electrons. These conditions can be written as

$$\int_{\gamma_{\text{min}}}^{\gamma_{\text{max}}} \dot{N}(\gamma) d\gamma = \eta_e \dot{N}_{\text{in}} \quad , \quad (15)$$

$$\int_{\gamma_{\text{min}}}^{\gamma_{\text{max}}} \gamma m_e c^2 \dot{N}(\gamma) d\gamma = \xi_e \frac{3}{2} kT \dot{N}_{\text{in}} \quad . \quad (16)$$

One can solve these two equations numerically for N_0 and γ_{min} , given p , γ_{max} , η_e and ξ_e . For our fiducial parameter set, γ_{min} is much smaller than γ_{max} and if $p > 2$ it is approximately given by,

$$\begin{aligned} \gamma_{\text{min}} &\approx \frac{3(p-2)kT}{2(p-1)\eta_e m_e c^2} \\ &= 8.4 \frac{(p-2)\xi_{e,-2}}{(p-1)\eta_{e,-5}} f_{\text{T}} M_{14}^{2/3} w(z)^{1/3} (1+z) \quad , \quad (17) \end{aligned}$$

where $\xi_{e,-2} = (\xi_e/0.01)$ and $\eta_{e,-5} = (\eta_e/10^{-5})$. For our fiducial parameters, this approximate formula is accurate enough as long as $p > 2.2$. Finally, for convenience, Eq. (16) can be written as,

$$N_0 m_e c^2 = \frac{\xi_e}{f(p)} \frac{3}{2} kT \frac{(\Omega_{\text{b}}/\Omega_{\text{m}})\dot{M}}{\mu m_p} \quad , \quad (18)$$

where

$$f(p) = \begin{cases} \ln(\gamma_{\text{max}}/\gamma_{\text{min}}) & (p=2) \\ \frac{1}{p-2} \gamma_{\text{min}}^{2-p} [1 - (\gamma_{\text{min}}/\gamma_{\text{max}})^{p-2}] & (p \neq 2) \end{cases} \quad . \quad (19)$$

2.3 Spectrum of IC emission

Next we derive analytically the radiation spectrum of the IC emission for a power-law distribution of injected electrons given by Eq. (10). A similar analysis has been done for synchrotron radiation in the study of gamma-ray bursts (e.g., Sari, Piran, & Narayan 1998).

The radiation power and the characteristic frequency of upscattered CMB photons which is radiated from a relativistic electron with Lorentz factor γ are (Blumenthal & Gould 1970),

$$P(\gamma) = \frac{4}{3} \sigma_{\text{T}} c \gamma^2 \frac{B_{\text{CMB}}^2}{8\pi} \quad , \quad (20)$$

$$\begin{aligned} \nu(\gamma) &= \frac{4}{3} \gamma^2 \bar{\nu}_{\text{CMB}} \\ &= 2.05 \times 10^{11} \gamma^2 (1+z) \text{ Hz} \quad , \quad (21) \end{aligned}$$

where $h\bar{\nu}_{\text{CMB}} \approx 2.70 kT_{\text{CMB}}$ is the mean energy of CMB photons and we adopt $T_{\text{CMB}} = 2.726 (1+z) \text{ K}$ (Fixsen 2009). The spectral power, P_ν (power per unit frequency, in

units of $\text{ergs s}^{-1} \text{Hz}^{-1}$), is proportional to ν for $\nu < \nu(\gamma)$ and cuts off sharply at $\nu > \nu(\gamma)$. The function P_ν is peaked around $\nu(\gamma)$, and its peak value is well approximated as $P_{\nu,\text{max}} \approx P(\gamma)/\nu(\gamma)$. Note that $P_{\nu,\text{max}}$ is independent of γ .

The above description of P_ν is only suitable when the electron does not lose a significant fraction of its energy to radiation. This requires the characteristic cooling time of the electrons to be longer than the dynamical time of a cluster, which is given by,

$$t_{\text{dyn}} = \frac{r_{\text{vir}}}{V_c} = 1.5 w(z)^{-1/2} (1+z)^{-3/2} \text{ Gyr} \quad . \quad (22)$$

Otherwise, the effect of energy loss must be considered. The energy loss rate of electrons is dominated by Coulomb collisions at low energies and synchrotron and IC losses at high energies (Sarazin 1999; Petrosian et al. 2008). The cooling time via Coulomb collisions is well approximated for relativistic electrons as,

$$t_{\text{Cmb}}(\gamma) = \frac{2}{3\sigma_{\text{T}} c n_e \ln \Lambda} \gamma \quad . \quad (23)$$

In the following, we assume that the electron density downstream of the shock is $n_e \approx 0.5 n_g$, where the factor 0.5 represents the number fraction of electrons to total gas particles, and the gas density n_g is given in Eq. (8). For simplicity, we fix a Coulomb logarithm at a value $\ln \Lambda = 40$. The synchrotron and IC cooling times have been already derived in Eq. (12). One can find the Lorentz factors, γ_{b1} , γ_{b2} and γ_{b3} , at which two of the three timescales, $t_{\text{IC/syn}}(\gamma)$, $t_{\text{IC/syn}}(\gamma)$ and t_{dyn} , are balanced, such that,

$$t_{\text{IC/syn}}(\gamma_{\text{b1}}) = t_{\text{dyn}} \quad (24)$$

$$t_{\text{Cmb}}(\gamma_{\text{b2}}) = t_{\text{IC/syn}}(\gamma_{\text{b2}}) \quad (25)$$

$$t_{\text{Cmb}}(\gamma_{\text{b3}}) = t_{\text{dyn}} \quad (26)$$

Since $t_{\text{IC/syn}} \propto \gamma^{-1}$, $t_{\text{Cmb}} \propto \gamma$ and $t_{\text{dyn}} \propto \gamma^0$, γ_{b2} is always between γ_{b1} and γ_{b3} . Electrons with Lorentz factor γ do not suffer significant cooling only if $\gamma_{\text{b3}} < \gamma < \gamma_{\text{b1}}$.

To find the spectral shape of the IC emission taking into account the electron cooling, we define characteristic frequencies as,

$$\nu_{\text{bi}} = \nu(\gamma_{\text{bi}}) \quad , \quad i = 1, 2, 3 \quad (27)$$

and obtain,

$$\nu_{\text{b1}} = 4.8 \times 10^{17} \frac{w(z)(1+z)^{-4}}{[1 + (B/B_{\text{CMB}})^2]^2} \text{ Hz} \quad , \quad (28)$$

$$\nu_{\text{b2}} = 2.9 \times 10^{15} \left(\frac{\ln \Lambda}{40}\right) \frac{r_4 f_{\text{acc}} w(z)}{1 + (B/B_{\text{CMB}})^2} \text{ Hz} \quad , \quad (29)$$

$$\nu_{\text{b3}} = 1.8 \times 10^{13} \left(\frac{\ln \Lambda}{40}\right)^2 r_4^2 f_{\text{acc}}^2 w(z)(1+z)^4 \text{ Hz} \quad . \quad (30)$$

These three frequencies coincide at a redshift z_{eq} approximately given by,

$$1 + z_{\text{eq}} \approx 3.6 \left(\frac{\ln \Lambda}{40}\right)^{-1/4} (r_4 f_{\text{acc}})^{-1/4} \quad , \quad (31)$$

where the term $(B/B_{\text{CMB}})^2$ is small and hence neglected [see Eq. (14)]. One can see $\nu_{\text{b3}} < \nu_{\text{b2}} < \nu_{\text{b1}}$ for $z < z_{\text{eq}}$ and $\nu_{\text{b1}} < \nu_{\text{b2}} < \nu_{\text{b3}}$ for $z > z_{\text{eq}}$. The spectral shapes are different for these two cases, and are treated separately in the following. Our results are summarized in Figure 1.

2.3.1 IC spectrum for $\nu_{b3} < \nu_{b2} < \nu_{b1}$

An electron with an initial Lorentz factor $\gamma > \gamma_{b1}$ cools down to γ_{b1} in the dynamical time t_{dyn} . Recall that the peak value of the instantaneous emissivity, $P_{\nu, \text{max}}$, is independent of the electron energy. Thus, the average emission power at frequency ν is proportional to the cooling time of electrons with Lorentz factor γ , satisfying $\nu = \nu(\gamma) \propto \gamma^2$. Therefore, the average spectrum scales as¹ $P_{\nu} \propto t_{\text{IC/syn}}(\gamma) \propto \nu^{-1/2}$ for $\nu_{b1} < \nu < \nu(\gamma)$. For $\nu < \nu_{b1}$, the spectrum has a low-energy tail, $P_{\nu} \propto \nu$. For $\nu > \nu(\gamma)$, the spectrum steeply decays. The averaged spectrum from such electrons has a peak at ν_{b1} .

An electron with an initial Lorentz factor $\gamma_{b3} < \gamma < \gamma_{b1}$ does not suffer significant cooling, and the radiation spectrum is $P_{\nu} \propto \nu$ for $\nu < \nu(\gamma)$ with a sharp cut off for $\nu > \nu(\gamma)$. An electron with an initial Lorentz factor $\gamma < \gamma_{b3}$ suffer energy loss via Coulomb loss, so that we obtain $P_{\nu} \propto t_{\text{Climb}}(\gamma) \propto \nu^{1/2}$ for $\nu < \nu(\gamma)$ with sharp cutoff for $\nu > \nu(\gamma)$.

To calculate the net spectrum from a power-law distribution of electrons, one needs to integrate over γ . There are three different cases, depending on γ_{min} , in which (A) $\gamma_{b3} < \gamma_{b1} < \gamma_{\text{min}}$, (B) $\gamma_{b3} < \gamma_{\text{min}} < \gamma_{b1}$ and (C) $\gamma_{\text{min}} < \gamma_{b3} < \gamma_{b1}$. Below we provide additional details on these regimes.

- (A) $\gamma_{b3} < \gamma_{b1} < \gamma_{\text{min}}$ (i.e., $\nu_{b3} < \nu_{b1} < \nu_{\text{m}}$):

In this case, all the electrons cool down to γ_{b1} . The spectral power is given by,

$$\nu L_{\nu} = \begin{cases} L_0(\nu/\nu_{\text{m}})^{(2-p)/2} & (\text{A1: } \nu_{\text{m}} < \nu) \\ L_0(\nu/\nu_{\text{m}})^{1/2} & (\text{A2: } \nu_{b1} < \nu < \nu_{\text{m}}) \\ L_0(\nu_{\text{m}}/\nu_{b1})^{3/2}(\nu/\nu_{\text{m}})^2 & (\text{A3: } \nu < \nu_{b1}) \end{cases}, \quad (32)$$

where,

$$\nu_{\text{m}} = \nu(\gamma_{\text{min}}). \quad (33)$$

To determine the normalization constant, L_0 , one can use the fact that electrons with $\gamma > \gamma_{b1}$ lose almost all their energy via IC emission, that is, the luminosity in the regime $\nu_{\text{m}} < \nu$ can be written as (Loeb & Waxman 2000; Keshet et al. 2003; Kushnir & Waxman 2009),

$$L_{\nu} d\nu = \gamma m_e c^2 \dot{N}(\gamma) d\gamma. \quad (34)$$

Using Eqs. (10) and (18) and $d\nu/\nu = 2d\gamma/\gamma$ for $\nu \propto \gamma^2$, we obtain,

$$\begin{aligned} L_0 &= \frac{3\xi_e kT}{4g(p)} \frac{(\Omega_b/\Omega_m)\dot{M}}{\mu m_p} \\ &= 2.0 \times 10^{43} \frac{f_{\text{T}} f_{\text{acc}} \xi_e - 2}{g(p)} M_{14}^{5/3} w(z)^{5/6} (1+z)^{5/2} \text{erg s}^{-1} \quad (35) \end{aligned}$$

where,

$$g(p) = \begin{cases} \ln(\gamma_{\text{max}}/\gamma_{\text{min}}) & (p=2) \\ \frac{1}{p-2} [1 - (\gamma_{\text{min}}/\gamma_{\text{max}})^{p-2}] & (p \neq 2) \end{cases}. \quad (36)$$

- (B) $\gamma_{b3} < \gamma_{\text{min}} < \gamma_{b1}$ (i.e., $\nu_{b3} < \nu_{\text{m}} < \nu_{b1}$):

In this case, only those electrons with $\gamma > \gamma_{b1}$ can cool. We have,

$$\nu L_{\nu} = \begin{cases} L_0(\nu/\nu_{\text{m}})^{(2-p)/2} & (\text{B1: } \nu_{b1} < \nu) \\ L_0(\nu_{\text{m}}/\nu_{b1})^{1/2}(\nu/\nu_{\text{m}})^{(3-p)/2} & (\text{B2: } \nu_{\text{m}} < \nu < \nu_{b1}) \\ L_0(\nu_{\text{m}}/\nu_{b1})^{1/2}(\nu/\nu_{\text{m}})^2 & (\text{B3: } \nu < \nu_{\text{m}}) \end{cases}, \quad (37)$$

where L_0 is given by Eq. (35).

- (C) $\gamma_{\text{min}} < \gamma_{b3} < \gamma_{b1}$ (i.e., $\nu_{\text{m}} < \nu_{b3} < \nu_{b1}$):

In this case, electrons with $\gamma > \gamma_{b1}$ and $\gamma < \gamma_{b3}$ can cool. The electron spectrum has a break at γ_{b3} , below which it is well approximated with the stationary solution, $\propto \dot{N}(\gamma) t_{\text{Climb}}(\gamma) \propto \gamma^{1-p}$ (Sarazin 1999). Hence, we have $L_{\nu} \propto \nu^{(2-p)/2}$ for $\nu_{\text{m}} < \nu < \nu_{b3}$. Therefore, the luminosity is given by,

$$\nu L_{\nu} = \begin{cases} L_0(\nu/\nu_{\text{m}})^{(2-p)/2} & (\text{C1: } \nu_{b1} < \nu) \\ L_0(\nu_{\text{m}}/\nu_{b1})^{1/2}(\nu/\nu_{\text{m}})^{(3-p)/2} & (\text{C2: } \nu_{b3} < \nu < \nu_{b1}) \\ L_0(\nu_{\text{m}}/\nu_{b1})^{1/2}(\nu_{\text{m}}/\nu_{b3})^{1/2}(\nu/\nu_{\text{m}})^{(4-p)/2} & (\text{C3: } \nu_{\text{m}} < \nu < \nu_{b3}) \\ L_0(\nu_{\text{m}}/\nu_{b1})^{1/2}(\nu_{\text{m}}/\nu_{b3})^{1/2}(\nu/\nu_{\text{m}})^{3/2} & (\text{C4: } \nu < \nu_{\text{m}}) \end{cases}$$

where L_0 is given by Eq. (35).

2.3.2 IC spectrum for $\nu_{b1} < \nu_{b2} < \nu_{b3}$

In this case, the electrons suffer significant cooling throughout. Hence, an electron with an initial Lorentz factor $\gamma > \gamma_{b2}$ cools down through γ_{b2} until which it produces $P_{\nu} \propto \nu^{-1/2}$, and further lose its energy to form $P_{\nu} \propto \nu^{1/2}$ below ν_{b2} . The average spectrum from such electrons has a peak at ν_{b2} . Similarly, an electron with an initial Lorentz factor $\gamma < \gamma_{b2}$ produces the average spectrum $P_{\nu} \propto \nu^{1/2}$ for $\nu < \nu(\gamma)$. In calculating the net spectrum for power-law electron distribution, there are two different cases in which (D) $\gamma_{b2} < \gamma_{\text{min}}$ and (E) $\gamma_{\text{min}} < \gamma_{b2}$. Below we describe them in detail.

- (D) $\gamma_{b2} < \gamma_{\text{min}}$ (i.e., $\nu_{b2} < \nu_{\text{m}}$):

Electrons with $\gamma > \gamma_{\text{min}}$ cools to make a spectrum $L_{\nu} \propto \nu^{-p/2}$ for $\nu > \nu_{\text{m}}$, while electrons with γ_{min} forms the spectrum below ν_{m} . The luminosity is given by,

$$\nu L_{\nu} = \begin{cases} L_0(\nu/\nu_{\text{m}})^{(2-p)/2} & (\text{D1: } \nu_{\text{m}} < \nu) \\ L_0(\nu/\nu_{\text{m}})^{1/2} & (\text{D2: } \nu_{b2} < \nu < \nu_{\text{m}}) \\ L_0(\nu_{\text{m}}/\nu_{b2})(\nu/\nu_{\text{m}})^{3/2} & (\text{D3: } \nu < \nu_{b2}) \end{cases}, \quad (39)$$

where L_0 is given by Eq. (35).

- (E) $\gamma_{\text{min}} < \gamma_{b2}$ (i.e., $\nu_{\text{m}} < \nu_{b2}$):

In this case, electron distribution for $\gamma_{\text{min}} < \gamma < \gamma_{b2}$ is proportional to $\dot{N}(\gamma) t_{\text{Climb}}(\gamma) \propto \gamma^{1-p}$. Hence, we have,

$$\nu L_{\nu} = \begin{cases} L_0(\nu/\nu_{\text{m}})^{(2-p)/2} & (\text{E1: } \nu_{b2} < \nu) \\ L_0(\nu_{\text{m}}/\nu_{b2})(\nu/\nu_{\text{m}})^{(4-p)/2} & (\text{E2: } \nu_{\text{m}} < \nu < \nu_{b2}) \\ L_0(\nu_{\text{m}}/\nu_{b2})(\nu/\nu_{\text{m}})^{3/2} & (\text{E3: } \nu < \nu_{\text{m}}) \end{cases}, \quad (40)$$

where L_0 is given by Eq. (35).

2.4 Observed surface brightness of IC emission

The observed surface brightness S_{ν} (in units of $\text{erg s}^{-1} \text{cm}^{-2} \text{Hz}^{-1} \text{str}^{-1}$) of IC emission from a cluster at redshift z is given by,

¹ This spectral slope is identical to the similar case considered in Sari, Piran, & Narayan (1998) since both of the characteristic frequencies of the synchrotron and IC emissions are proportional to the square of the electron energy.

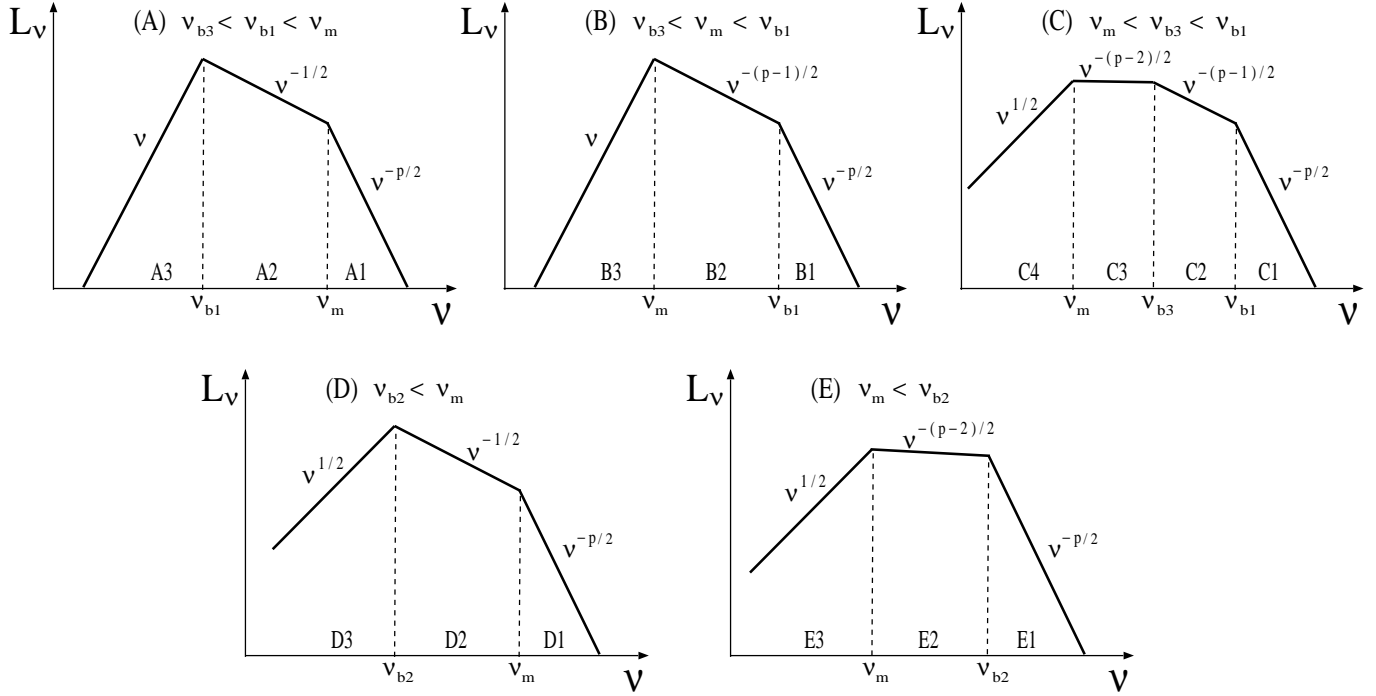


Figure 1. IC Spectrum from power-law distribution of relativistic electrons. Regimes (A) $\nu_{b3} < \nu_{b1} < \nu_m$, (B) $\nu_{b3} < \nu_m < \nu_{b1}$ and (C) $\nu_m < \nu_{b3} < \nu_{b1}$ are for $\nu_{b3} < \nu_{b2} < \nu_{b1}$, while regimes (D) $\nu_{b2} < \nu_m$ and (E) $\nu_m < \nu_{b2}$ are for $\nu_{b1} < \nu_{b2} < \nu_{b3}$.

$$S_\nu = \frac{(1+z)L_{\nu_s}}{4\pi d_L(z)^2 \Omega_\nu}, \quad (41)$$

where $\nu_s = (1+z)\nu$, $d_L(z)$ and Ω_ν are the observing frequency translated into the cluster rest frame, the luminosity distance to the cluster and the solid angle of the extended emission on the sky, respectively.

The *effective* value of Ω_ν can be estimated based on the observed brightness profile in the sky, which depends on the Lorentz factor of the electrons, $\gamma_\nu = (\nu/2.05 \times 10^{11} \text{ Hz})^{1/2}$, emitting IC photons with observed frequency ν [see Eq. (21)]. If the total cooling time of such electrons, $t_{\text{cool}}(\gamma_\nu) = [t_{\text{IC/syn}}(\gamma_\nu)^{-1} + t_{\text{Cmb}}(\gamma_\nu)^{-1}]^{-1}$, is much smaller than the dynamical time of the cluster t_{dyn} , then the emission mainly originates from the region around the shock. The width of the emission region (in the radial direction) is given by the product of downstream flow velocity and the cooling time, $\delta \sim (1/3)V_c t_{\text{cool}}(\gamma_\nu) < r_{\text{vir}}$, where a factor 1/3 applies to the strong shock limit. The surface brightness profile has a rim-brightened shape. Because of projection, the observed apparent scale width, W , in the sky differs from δ . The ratio W/δ depends on the uncertain radial profile of the electron distribution downstream of the shock, but is typically around 3 (Bamba et al. 2005a). Writing $W = f_W \delta$, we obtain $\Omega_\nu \approx 2\pi(f_W/3)r_{\text{vir}}V_c t_{\text{cool}}(\gamma_\nu)/d_A^2$, where d_A is the angular diameter distance to the cluster. On the other hand, if $t_{\text{cool}}(\gamma_\nu) \gg t_{\text{dyn}}$, the cluster interior is filled with electrons with γ_ν . Taking into account the projection effect, the surface brightness profile is center-filled. In this case, assuming the bright emission in the sky originates from inside the radius $r_{\text{vir}}/2$, it occupies a solid angle $\Omega_\nu \approx (\pi/4)(r_{\text{vir}}/d_A)^2$. Connecting both limits, we get

$$\Omega_\nu = \frac{\pi}{4} \left(\frac{r_{\text{vir}}}{d_A} \right)^2 \min \left\{ 1, 8 \frac{f_W}{3} \frac{t_{\text{cool}}(\gamma_\nu)}{t_{\text{dyn}}} \right\}. \quad (42)$$

3 RESULTS

Based on the derivations in the previous sections, we can now calculate the observed surface brightness S_ν in the SDSS g-band ($\nu = 6.3 \times 10^{14} \text{ Hz}$) as a function of redshift z and a halo mass M . Other parameters are fixed at the fiducial values, $p = 2.5$, $r_4 = \xi_{B,-2} = \eta_g = \eta_{e,-5} = 1$, $\xi_{e,-2} = 5$, $f_{\text{acc}} = f_T = 0.5$ and $f_W = 3$. The parameter η_e is highly uncertain and depends on upstream physical quantities such as magnetic field and gas temperature (e.g., Matsukiyo et al. 2011; Guo et al. 2014a,b). It can range from $\sim 10^{-7}$ to $\sim 10^{-4}$ (Kang et al. 2012). If η_e is so large, then γ_{min} is less than unity [see Eq. (17)], so that our assumption of single power-law spectrum breaks down. Dependence of η_e is easily found as seen in the following. The spectral index p is also uncertain, however recent study of particle acceleration at cluster shocks suggest $p \approx 2.25$ – 2.5 (Kang & Ryu 2011, 2013; Hong et al. 2014; Guo et al. 2014a). In the following, we also consider the cases of $p = 2.0$, 2.3 and 3.0 , as well as the fiducial case of $p = 2.5$. The index p is related to the shock compression ratio r . For first-order Fermi acceleration, $p = (r+2)/(r-1)$ in the test-particle limit (Blandford & Ostriker 1978; Bell 1978). In this case, r ranges between 2.5 and 4 for $2 < p < 3$. Nevertheless, we fix $r_4 = (r/4) = 1$, which corresponds to the strong shock limit, because observed surface brightness does not depend on r for the parameters of interest. All the equations in this section do not depend on r .

Figure 2 shows the surface brightness as a function of

redshift z , for a fixed halo mass $M_{14} = (M/10^{14}M_\odot) = 3$. The red line describes the fiducial value of $p = 2.5$, while the others are for different values of p with the other parameters fixed at their fiducial values. Interestingly, the surface brightness increases with z . At low redshifts where the effects of cosmological expansion are negligible, the brightness is almost constant, ≈ 36 mag arcsec $^{-2}$. As z increases, the surface brightness becomes larger by ≈ 3 mag until $z \approx 2$. For this redshift range, one can see from Figure 3, that $\nu_{b3} < \nu_m < \nu_s = (1+z)\nu < \nu_{b1}$, so that the spectrum is in the regime B2 [see Eq. (37)]. Thus, we find,

$$\begin{aligned} L_{\nu_s} &= L_0 \nu_{b1}^{-1/2} \nu_m^{(p-2)/2} \nu_s^{(1-p)/2} \\ &\propto f_{\text{acc}} f_{\text{T}}^{p-1} \xi_e^{p-1} \eta_e^{2-p} M_{14}^{(2p+1)/3} \\ &\quad \times w(z)^{(p-1)/3} (1+z)^{3(p+1)/2} \nu_s^{(1-p)/2}. \end{aligned} \quad (43)$$

Since electron cooling is not significant, the solid angle of the emission is given by $\Omega_\nu \approx (\pi/4)(r_{\text{vir}}/d_A)^2$, so that,

$$\begin{aligned} S_\nu &\propto r_{\text{vir}}^{-2} (1+z)^{-3} L_{\nu_s} \\ &\propto f_{\text{acc}} f_{\text{T}}^{p-1} \xi_e^{p-1} \eta_e^{2-p} M_{14}^{(2p-1)/3} \\ &\quad \times w(z)^{(p+1)/3} (1+z)^{p+1} \nu^{(1-p)/2}. \end{aligned} \quad (44)$$

Since $w(z)$ is only weakly dependent on z , the surface brightness S_ν increases with z following the scaling $(1+z)^{p+1}$.

The regime B2 ends when ν_s becomes larger than ν_{b1} . This crossing occurs at $z \approx 2$ for our fiducial parameters. Thereafter, the spectrum is in regime B1. When z further increases, the spectrum enters into regime A1, subsequently followed by the regime D1. In these regimes, the luminosity is given by the same form [see Eqs. (32), (37) and (39)],

$$\begin{aligned} L_{\nu_s} &= L_0 \nu_m^{(p-2)/2} \nu_s^{-p/2} \\ &\propto f_{\text{acc}} f_{\text{T}}^{p-1} \xi_e^{p-1} \eta_e^{2-p} M_{14}^{(2p+1)/3} \\ &\quad \times w(z)^{(2p+1)/6} (1+z)^{(3p-1)/2} \nu_s^{-p/2}, \end{aligned} \quad (45)$$

and the solid angle is still given by $\Omega_\nu \approx (\pi/4)(r_{\text{vir}}/d_A)^2$, so that we have,

$$\begin{aligned} S_\nu &\propto f_{\text{acc}} f_{\text{T}}^{p-1} \xi_e^{p-1} \eta_e^{2-p} M_{14}^{(2p-1)/3} \\ &\quad \times w(z)^{(2p+5)/6} (1+z)^{(2p-3)/2} \nu^{-p/2}. \end{aligned} \quad (46)$$

For our fiducial parameters, Eq. (46) describes the scaling if $2 < z < 5.1$. The flux increases by a factor of about 3 in this redshift range. Note that the emergence of these regimes originates from rapid decreasing of $\nu_{b1} \propto (1+z)^{-4}$ for $z > 1$. As a result, the blue-shifted observing frequency $\nu_s = (1+z)\nu$ becomes larger than any other characteristic frequencies, ν_m and ν_{bi} ($i = 1, 2, 3$), around z_{eq} . As z further increases, $\nu_m \propto (1+z)^2$ together with $\nu_{b3} \propto (1+z)^4$ become large, finally exceeding ν_s , so that the spectrum enters the regime D2. There the electron cooling is so significant that the observed brightness profile is rim-brightened shape, so that Ω_ν is small and S_ν shows rapid increase for $z \gtrsim 6$. However, the abundance of clusters at these high redshifts is extremely small (Barkana & Loeb 2001; Watson et al. 2013).

Although the parameter dependence is somewhat complicated, one can see that overall behavior is not so different from the fiducial parameter set; the brightness varies typically by up to ≈ 2 –3 mag if one of parameters is changed with others fixed. Figure 2 shows lines for the cases of $p = 2.0, 2.3$ and 3.0 with other parameters fixed as fiducial. The larger the p , the brighter the surface emission. The de-

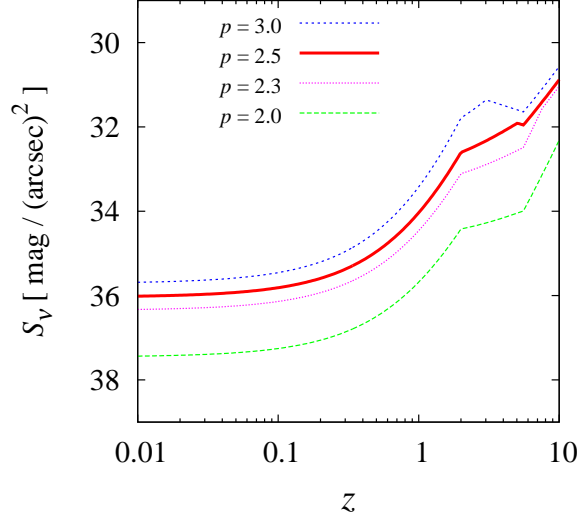


Figure 2. Observed SDSS g-band surface brightness of IC emission from a cluster with $M_{14} = 3$ (in units of mag arcsec $^{-2}$) as a function of cluster redshift z . The red line is for fiducial parameters ($p = 2.5$, $r_4 = \xi_{B,-2} = \eta_g = \eta_{e,-5} = 1$, $\xi_{e,-2} = 5$, $f_{\text{acc}} = f_{\text{T}} = 0.5$ and $f_{\text{W}} = 3$), while the green, purple and blue lines are for $p = 2.0, 2.3$ and 3.0 , respectively.

pendence on other parameters can be found from Eqs. (44) and (46).

Figure 4 depicts the surface brightness as a function of a halo mass M for fixed cluster redshifts assuming the fiducial parameter values. As seen in Fig. 2, the redshift dependence is small when $z \lesssim 0.1$. There, the surface brightness peaks at $M_{14} \approx 30$, below which the spectrum is in regime B2 for $0.55 \lesssim M_{14} \lesssim 30$ and in regime C2 for $M_{14} \lesssim 0.55$. Functional forms of the brightness for B2 and C2 are given by Eq. (44), with $S_\nu \propto M_{14}^{(2p-1)/3}$. For $M_{14} \gtrsim 30$ the spectrum is in regime B3, at which we have,

$$S_\nu \propto f_{\text{acc}} f_{\text{T}}^{-2} \xi_e^{-2} \eta_e^3 M_{14}^{-1} w(z) \nu, \quad (47)$$

so that the brightness decreases with M . For $z = 0.5$, the peak shifts to lower masses, and larger values. Note that Eq. (47) implies that the brightness in regime B3 very weakly depends on z . The behavior for $z = 1.3$ is the same as for lower redshifts as long as $M_{14} < 33$, above which, however, the spectrum is in the regime A3 and the surface brightness again increases with M and z according to the scaling,

$$S_\nu \propto f_{\text{acc}} \eta_e M_{14}^{1/3} w(z)^{1/3} (1+z)^7 \nu. \quad (48)$$

For higher redshifts $z = 2.0$ ($z = 4.0$), the spectrum enters regimes C2, B2 and B1 (E1 and D1) in turn towards higher

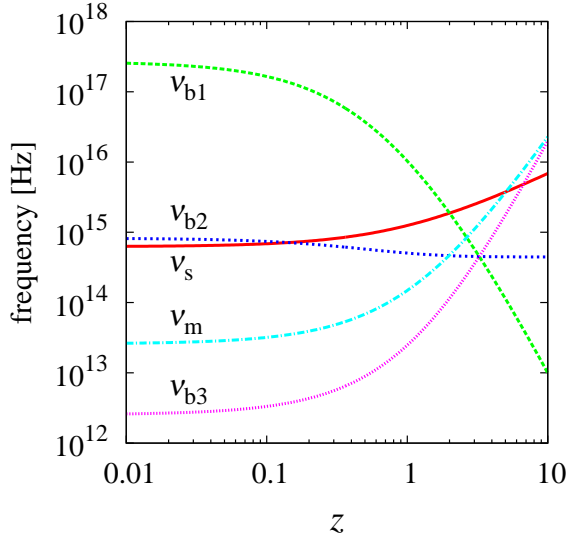


Figure 3. Characteristic frequencies, as measured in the rest frame of a cluster, for our fiducial parameter values with a halo mass $M_{14} = 3$, as a function of redshift z . The green, blue, purple and light blue lines indicate ν_{b1} , ν_{b2} , ν_{b3} and ν_m , respectively. The red line represents $\nu_s = (1+z)\nu$, which is the observed frequency blue-shifted to the rest frame of the cluster.

M . The brightness breaks at $M_{14} = 8.5$ and 3.9 for $z = 2.0$ and 4.0 , respectively. After the break, the brightness still increases with M according to the scaling,

$$S_\nu \propto f_{\text{acc}} \eta_e M_{14}^{1/3} w(z)^{7/6} (1+z)^{-1/2} \nu^{-1/2}. \quad (49)$$

In summary, the surface brightness follows simple scaling behavior, $S_\nu \propto M^{(2p-1)/3}$, for the typical range of expected parameters.

4 DISCUSSION

Using a simple analytical model, we have calculated IC emission in the SDSS g-band from relativistic electrons accelerated in galaxy clusters, taking into account the effects of Coulomb, synchrotron, and IC energy loss of the emitting electrons. For our fiducial parameters, at $z \lesssim 2$ and $M \lesssim 10^{15} M_\odot$, the spectrum is in the regime B2 or C2, in which $S_\nu \propto M^{(2p-1)/3} (1+z)^{p+1} \nu^{(1-p)/2}$, where p is the power-law index of electron distribution (see Fig. 4). If the value of p is inferred from radio synchrotron emission, one can predict the spectral index of the optical IC emission. In this paper, we have not taken into account the possibility of reacceleration in the downstream turbulence, which enhances the abundance of relativistic electrons (Schlickeiser et al. 1987;

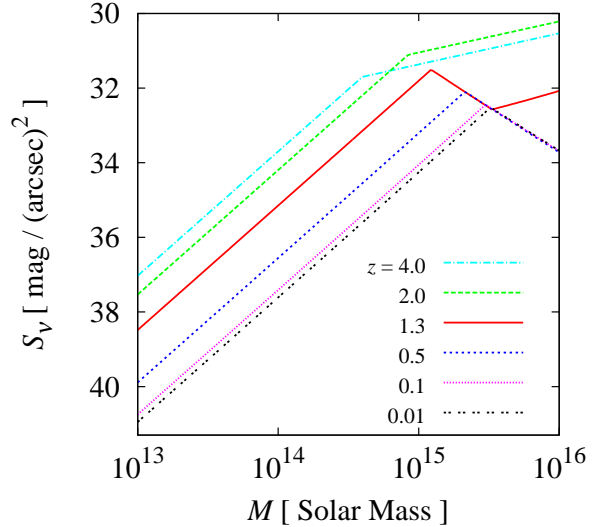


Figure 4. Observed SDSS g-band surface brightness (in units of mag arcsec^{-2}) as a function of a halo mass M for our fiducial parameters ($p = 2.5$, $r_4 = \xi_{B,-2} = \eta_g = \eta_{e,-5} = 1$, $\xi_{e,-2} = 5$, $f_{\text{acc}} = f_T = 0.5$ and $f_W = 3$). Different lines correspond to different redshifts z of the cluster.

Brunetti et al. 2001; Petrosian 2001; Fujita et al. 2003), resulting in brighter IC emission. We also assume a spherical, virialized shock as a result of smooth accretion. If the cluster is not dynamically relaxed and is still being formed, e.g. as a result of a merger of two sub-components, then the shock structure would be different and turbulent energy would be enhanced. In this case, we expect brighter IC emission due to more efficient reacceleration. Hence, our estimate for the IC flux and surface brightness should be regarded as a conservative lower limit.

It would be natural to assume that electron acceleration occurs at the virial shocks. In merging clusters, radio relics have been detected as possible signatures of the merger shocks, although clear evidence for it had not been identified as of yet. Observations at other wavelengths would be helpful for shock identification. Proton acceleration at the virial shocks could also occur, although we have only a few observational implications of it (e.g., Fujita et al. 2013). Observations of optical IC emission may have the advantage of enabling the identification of shocks, because the angular resolution of the optical telescopes is generally much better than hard X-ray or gamma-ray telescopes. According to the theory of diffusive shock acceleration, electrons responsible for the optical IC emission cannot penetrate far upstream relative to the shock front. Hence, the IC emissivity

is expected to have a steep rise across the shock front. The detection of such a sharp jump in the IC emission would flag the position of the shock front, and provide evidence for particle acceleration there. In our spherical model, however, IC-emitting electrons are not rapidly cooling in most cases, resulting in center-filled shape of the brightness profile on the sky. Thus, the profile may not have a sharp rise in projection. Possible exceptions might be expected for more realistic, non-spherical cases, where sharp feature could be found on the sky at the location of shocks. Detailed morphological studies based on numerical simulations, like the case of radio relics (e.g., Skillman et al. 2013; Hong et al. 2015), are needed in this case and go beyond the scope of this paper.

Our model predicts the surface brightness of IC emission from several massive clusters, as summarized in Table 1. Larger fluxes are expected for larger M and z if the spectrum is in regime B2 or C2 [see Eq. (44)]. The predicted brightness ranges between ≈ 32 and 35 mag arcsec $^{-2}$. Such ultralow surface brightnesses should be detectable with the recently developed Dragonfly Telephoto Array (Abraham & van Dokkum 2014). More detailed prospects for the observation of individual clusters will be given elsewhere.

Our model also predicts the color of the IC emission, which is bluer than starlight. If we assume a power-law form of the IC emission, as $S_\nu \propto \nu^{-\alpha}$, then the color $g - r$ is calculated as

$$g - r = \frac{5}{2}\alpha \log_{10}(\nu_g/\nu_r) = 0.29\alpha, \quad (50)$$

where $\nu_g = 6.3 \times 10^{14}$ Hz and $\nu_r = 4.8 \times 10^{14}$ Hz are SDSS g-band and r-band frequencies, respectively. In the case of spectral regime B2 or C2 (i.e., $\alpha = (p - 1)/2$), we obtain $g - r = 0.19$ for $p = 2.3$. If the spectral regime is in B3 (i.e., $\alpha = -1$), then $g - r = -0.29$. These values are distinguishable from stellar components, such as diffuse faint emission of brightest cluster galaxies (BCG), satellite galaxies, and intracluster light (ICL), which typically shows $g - r \gtrsim 0.7$ (e.g., Montes & Trujillo 2014).

Gamma-ray and hard X-ray observations have given upper limits, which constrain our model parameters. Figures 5 and 6 show that for our fiducial parameters (namely $p = 2.5$), both IC gamma-ray and X-ray fluxes for nearby ($z \ll 0.1$), massive ($M_{14} = 30$) clusters exceed current observational upper limits, which are $N(0.2 - 100 \text{ GeV}) \lesssim 10^{-9} - 10^{-8}$ photons cm $^{-2}$ s $^{-1}$ for gamma-rays (Ackermann et al. 2010) and $F(12 - 60 \text{ keV}) \lesssim 10^{-11} - 10^{-10}$ erg cm $^{-2}$ s $^{-1}$ for X-rays (Ota et al. 2014). Although the case with $p \lesssim 2.5$ is unlikely for such nearby massive clusters, our model predictions can be lower than these current observational upper limits for less massive ($M_{14} \lesssim 10$), higher redshift ($z \gtrsim 0.1$) or steeper electron index ($p \gtrsim 2.8$)². Note that we conservatively adopt $p = 2.5$ in this paper, but that higher values of p as implied by the gamma-ray and X-ray limits for low red-

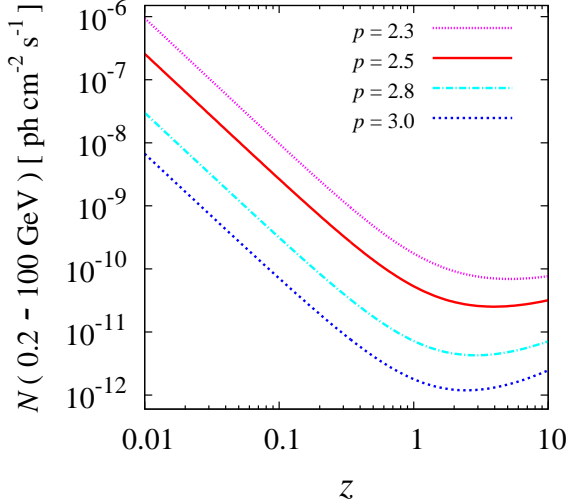


Figure 5. Observed IC gamma-ray flux $N(0.2 - 100 \text{ GeV})$, in units of photons cm $^{-2}$ s $^{-1}$, as a function of redshift z for most massive ($M_{14} = 30$) clusters. The red line is for fiducial parameters ($p = 2.5$, $r_4 = \xi_{B,-2} = \eta_g = \eta_{e,-5} = 1$, $\xi_{e,-2} = 5$, $f_{\text{acc}} = f_T = 0.5$ and $f_W = 3$), while the purple, light blue and blue lines are for $p = 2.3$, 2.8 and 3.0 , respectively. Mass dependence of the gamma-ray flux is given by Eq. (45), as $N(0.2 - 100 \text{ GeV}) \propto M_{14}^{(2p+1)/3}$, because observed frequency blue-shifted to the rest frame, ν_s , is always larger than any other characteristic frequencies, ν_{b1} , ν_{b2} , ν_{b3} and ν_m . Observed upper limits for specific clusters lie $N(0.2 - 100 \text{ GeV}) \lesssim 10^{-9} - 10^{-8}$ photons cm $^{-2}$ s $^{-1}$ (Ackermann et al. 2010).

shift clusters would make our predicted optical IC flux somewhat higher (see Fig. 2). Another independent way to have lower gamma-ray flux is to adopt unusually large $\eta_g \gg 10^2$. In this case, γ_{max} is small enough to give spectral cutoff of IC emission at energy below the *Fermi* band.

The IC emission from the virial shock of clusters could be enhanced due to relativistic electrons produced in supernovae that gradually diffuse out of the cluster. The latter contribution depends on the star formation history and the diffusion time of relativistic electrons within the cluster. The diffusion time of electrons depends on the unknown configuration of magnetic fields. If the fields are radially aligned in the outer envelope of clusters (as expected from radial infall or the magneto-thermal instability; see e.g., Parrish et al. 2012), then the diffusion time there would be of order the light crossing time of the outer parts of the cluster, i.e. millions of years. The *Fermi* satellite has placed tight limits on this contribution in cluster cores based

² Some X-ray observations for specific clusters have provided tight upper limits, such as $F(12 - 60 \text{ keV}) < 5 \times 10^{-12}$ erg cm $^{-2}$ s $^{-1}$ (Nishino et al. 2010) for Perseus ($z = 0.018$ and $M_{200} = 1.2 \times 10^{15} M_\odot$), while our model overpredicts X-ray flux by a factor of 3 larger even for $p = 3.0$. In such cases, smaller value of ξ_e ($\lesssim 0.01$) may be required.

Table 1. Predicted surface brightness in SDSS g-band for specific clusters.

Name	z	M^a [$10^{14} M_\odot$]	Surface brightness ^b [mag arcsec ⁻²]			Reference
			$p = 2.0$	$p = 2.5$	$p = 3.0$	
IDCS J1426.5+3508	1.75	5.3	34.1 (C2)	32.1 (B2)	31.2 (B3)	Stanford et al. (2012)
SPT-CL J2106–5844	1.132	9.8	34.2 (B2)	32.1 (B2)	31.8 (B3)	Williamson et al. (2011)
ACT-CL J0102–4915	0.870	22.3	33.7 (B2)	32.1 (B3)	32.7 (B3)	Menanteau et al. (2012)
SPT-CL J2344–4243	0.596	25.0	34.0 (B2)	32.3 (B3)	32.8 (B3)	McDonald et al. (2012)
MS 1054–0321	0.83	12	34.4 (B2)	32.3 (B2)	32.0 (B3)	Jee et al. (2005)
SPT-CL J0658–5556	0.296	31.2	34.3 (B2)	32.5 (B3)	33.1 (B3)	Williamson et al. (2011)
XDCP J0044.0–2033	1.579	4.4	34.5 (C2)	32.6 (B2)	31.7 (B2)	Tozzi et al. (2015)
SPT-CL J2337–5942	0.775	10.5	34.7 (B2)	32.6 (B2)	31.9 (B3)	Williamson et al. (2011)
Coma	0.0232	27.8	35.0 (B2)	32.7 (B2)	32.9 (B3)	Kubo et al. (2007)
MACS J1206.2–0847	0.44	14.1	34.9 (B2)	32.8 (B2)	32.2 (B3)	Presotto et al. (2014)
Abell 2390	0.228	18	35.1 (B2)	32.9 (B2)	32.5 (B3)	Carlberg et al. (1996)
XLSSU J021744.1–034536	1.91	$\approx 2^c$	35.0 (C2)	33.3 (B2)	32.6 (B2)	Mantz et al. (2014)
Abell 2744	0.3064	70	33.4 (B2)	33.3 (B3)	33.9 (B3)	Montes & Trujillo (2014)

^a Values of M_{200} are taken from references.

^b For fiducial parameters other than p . Spectral regime is also shown in parentheses.

^c Since only M_{500} is given in Mantz et al. (2014), we estimate M_{200} assuming isothermal density distribution as $M_{200} = 1.58 M_{500}$.

on the lack of gamma-ray emission at 0.2–100 GeV there (Ackermann et al. 2010, 2014, see also Vazza et al. 2015).

Diffuse optical emission from Thomson scattering of starlight could be comparable to the IC emission. We roughly estimate the flux of the scattered light emission as,

$$\nu F_\nu^{(\text{sc})} \sim \frac{L_* \tau_T}{4\pi d_L(z)^2}, \quad (51)$$

where L_* is the bolometric stellar luminosity and τ_T is the optical depth for the Thomson scattering. The typical mass-to-light ratio within the virial radius r_{vir} is given by $M/L \approx 2.5 \times 10^2 M_\odot/L_\odot$ (e.g., Sheldon et al. 2009; Holland et al. 2015), so that $L_* \approx 1.6 \times 10^{45} M_{14} \text{ erg s}^{-1}$. The optical depth τ_T can be estimated as,

$$\begin{aligned} \tau_T &\sim n_e \sigma_T r_{\text{vir}} \\ &\sim 3.3 \times 10^{-4} r_4 f_{\text{acc}} M_{14}^{1/3} w(z)^{2/3} (1+z)^2. \end{aligned} \quad (52)$$

Note that this estimate may be upper limit since we implicitly assume that most of the energy of the starlight is contained in the SDSS g-band in the observer frame. In Figure 7, we show $F_\nu^{(\text{sc})}$ as a function of redshift z (green lines), comparing with the IC flux (red lines). One can see that the IC emission dominates if $M_{14} \gtrsim 3$. Since the spectrum of the scattered light is very different from that of the IC emission, color measurements can be used to distinguish between them.

The BCG and ICL could also constitute a diffuse background. The ICL emission has been calculated based on the cosmological simulation (e.g., Rudick et al. 2011; Laporte et al. 2013; Cui et al. 2014). According to the recent result by Cui et al. (2014), the ICL brightness could be around 30 mag arcsec⁻² at r_{vir} for the most massive clusters. On the other hand, many observations measure the brightness profile of the BCG+ICL only in the interior of clusters due to its faintness (e.g., Presotto et al. 2014; DeMaio et al. 2015). Extrapolating linearly the observed radial profile of BCG+ICL of a cluster MACS J1206.2–0847 (Presotto et al.

2014) to its virial radius of $r_{\text{vir}} \sim 2.3$ Mpc yields emission that is dimmer than ~ 35 mag arcsec⁻², so that IC emission is brighter for this cluster (see Table 1). Even if BCG+ICL has comparable brightness to the IC emission, their color difference can be used to separate them from each other.

IC emission also lies in infrared bands; however, the flux is rather small because typically $\nu_s < \nu_m$ (i.e., it is in regime B3). Furthermore, mid and far-infrared bands may be dominated by dust emission (Yamada & Kitayama 2005; Kitayama et al. 2009).

Finally, we remark on IC emission as a possible background emission for other purposes. For example, as already discussed above, the BCG+ICL brightness around the virial radius r_{vir} could be comparable to the IC emission. The surface brightness of dwarf galaxies (e.g., Herrmann et al. 2013) is also in some cases less than 32 mag arcsec⁻² at the periphery of the galaxies. The IC emission could confuse or disguise these different emissions from member galaxies in massive clusters.

ACKNOWLEDGMENTS

We thank Roberto Abraham, Yutaka Fujita, Hyesung Kang, Yutaka Ohira, Kouji Ohta, Dongsu Ryu, Lorenzo Sironi, Shuta Tanaka, Makoto Uemura and Pieter van Dokkum, for valuable comments. We also thank the anonymous referee for valuable comments to improve the paper. This work was supported in part by grant-in-aid from the Ministry of Education, Culture, Sports, Science, and Technology (MEXT) of Japan, No. 15K05088 (R. Y.) and NSF grant AST-1312034 (A. L.). R. Y. also thank ISSI (Bern) for support of the team “Physics of the Injection of Particle Acceleration at Astrophysical, Heliospheric, and Laboratory Collisionless Shocks”.

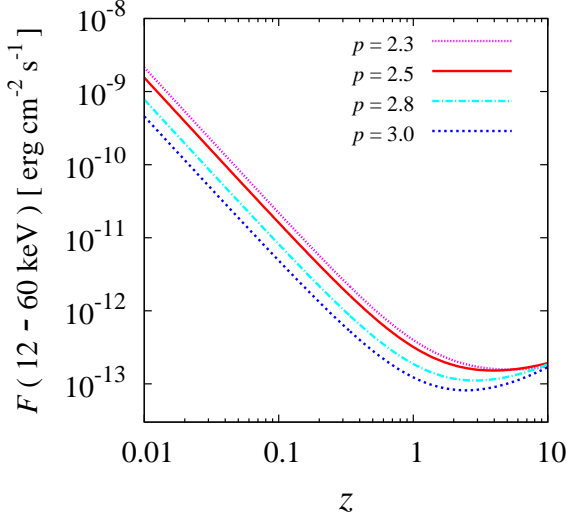


Figure 6. Observed IC X-ray flux $F(12 - 60 \text{ keV})$, in units of $\text{erg cm}^{-2} \text{ s}^{-1}$, as a function of redshift z for most massive ($M_{14} = 30$) clusters. The red line is for fiducial parameters ($p = 2.5$, $r_4 = \xi_{B,-2} = \eta_g = \eta_{e,-5} = 1$, $\xi_{e,-2} = 5$, $f_{\text{acc}} = f_{\text{T}} = 0.5$ and $f_{\text{W}} = 3$), while the purple, light blue and blue lines are for $p = 2.3, 2.8$ and 3.0 , respectively. Mass dependence of the gamma-ray flux is given by Eq. (45), as $F(12 - 60 \text{ keV}) \propto M_{14}^{(2p+1)/3}$, because observed frequency blue-shifted to the rest frame, ν_s , is always larger than any other characteristic frequencies, ν_{b1} , ν_{b2} , ν_{b3} and ν_m . Observed upper limits for specific clusters lie $F(12 - 60 \text{ keV}) \lesssim 10^{-11} - 10^{-10} \text{ erg cm}^{-2} \text{ s}^{-1}$ (Ota et al. 2014).

REFERENCES

- Abraham, R. G., & van Dokkum, P. G. 2014, *PASP*, 126, 55
- Ackermann, M., Ajello, M., Allafort, A., et al. 2010, *ApJL*, 717, L71
- Ackermann, M., Ajello, M., Albert, A., et al. 2014, *ApJ*, 787, 18
- Ade, P. A. R. et al. (Planck Collaboration) 2015, *arXiv:1502.01589*
- Bamba, A. et al. 2003, *ApJ*, 589, 827
- Bamba, A. et al. 2005a, *ApJ*, 621, 793
- Bamba, A. et al. 2005b, *ApJ*, 632, 294
- Bartels, R., Zandanel, F., & Ando, S. 2015, *A&A* in press (*arXiv:1501.06940*)
- Bell, A. R. 1978, *MNRAS*, 182, 147
- Barkana, R., & Loeb, A. 2001, *Phys. Rep.*, 349, 125
- Blandford, R. D., & Ostriker, J. P. 1978, *ApJ*, 221, L29
- Blasi, P., & Colafrancesco, S. 1999, *Astroparticle Physics*, 12, 169

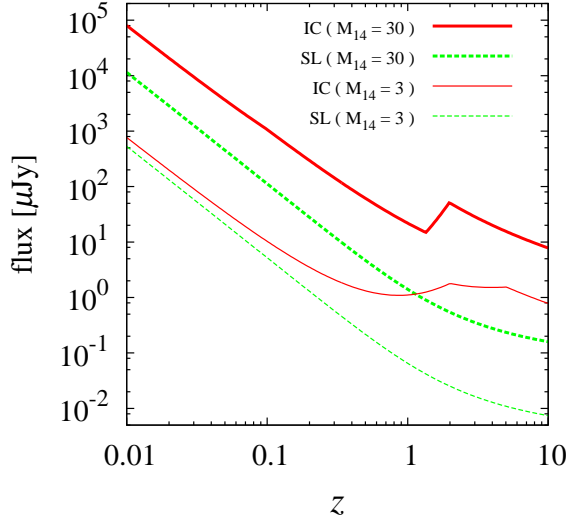


Figure 7. Observed SDSS g-band flux (in units of μJy) of IC emission (red lines) and the Thomson scattered starlight (green lines) as a function of redshift z . Thick and thin lines are for a halo mass $M_{14} = 30$ and $M_{14} = 3$, respectively. In calculating the IC flux, we adopt fiducial parameters ($p = 2.5$, $r_4 = \xi_{B,-2} = \eta_g = \eta_{e,-5} = 1$, $\xi_{e,-2} = 5$, $f_{\text{acc}} = f_{\text{T}} = 0.5$ and $f_{\text{W}} = 3$).

- Blumenthal, G. R., & Gould, R. J. 1970, *Reviews of Modern Physics*, 42, 237
- Brunetti, G., Setti, G., Feretti, L., & Giovannini, G. 2001, *MNRAS*, 320, 365
- Brunetti, G., & Jones, T. W. 2014, *Int. J. of Mod. Phys. D*, 23, 1430007
- Bryan, G. L., & Norman, M. L. 1998, *ApJ*, 495, 80
- Carlberg, R. G., Yee, H. K. C., Ellingson, E., et al. 1996, *ApJ*, 462, 32
- Cui, W., Murante, G., Monaco, P., et al. 2014, *MNRAS*, 437, 816
- DeMaio, T., Gonzalez, A. H., Zabludoff, A., Zaritsky, D., & Bradač, M. 2015, *MNRAS*, 448, 1162
- Drury, L. O'C., 1983, *Rep. Prog. Phys.*, 46, 973
- Fixsen, D. J. 2009, *ApJ*, 707, 916
- Fujita, Y., & Kato, T. N. 2005, *MNRAS*, 364, 247
- Fujita, Y., Ohira, Y., & Yamazaki, R. 2013, *ApJL*, 767, L4
- Fujita, Y., & Sarazin, C. L. 2001, *ApJ*, 563, 660
- Fujita, Y., Takizawa, M., & Sarazin, C. L. 2003, *ApJ*, 584, 190
- Gastaldello, F., Wik, D. R., Molendi, S., et al. 2015, *ApJ*, 800, 139
- Guo, X., Sironi, L., & Narayan, R. 2014a, *ApJ*, 794, 153
- Guo, X., Sironi, L., & Narayan, R. 2014b, *ApJ*, 797, 47

- Herrmann, K. A., Hunter, D. A., & Elmegreen, B. G. 2013, *AJ*, 146, 104
- Holland, J. G., Böhringer, H., Chon, G., & Pierini, D. 2015, *MNRAS*, 448, 2644
- Hong, S. E., Ryu, D., Kang, H., & Cen, R. 2014, *ApJ*, 785, 133
- Hong, S. E., Kang, H., & Ryu, D. 2015, *arXiv:1504.03102*
- Inoue, S., Aharonian, F. A., & Sugiyama, N. 2005, *ApJL*, 628, L9
- Jee, M. J., White, R. L., Ford, H. C., et al. 2005, *ApJ*, 634, 813
- Kang, H., & Ryu, D. 2011, *ApJ*, 734, 18
- Kang, H., Ryu, D., & Jones, T. W. 2012, *ApJ*, 756, 97
- Kang, H., & Ryu, D. 2013, *ApJ*, 764, 95
- Keshet, U., Waxman, E., Loeb, A., Springel, V., & Hernquist, L. 2003, *ApJ*, 585, 128
- Keshet, U., Waxman, E., & Loeb, A. 2004a, *JCAP*, 4, 006
- Keshet, U., Waxman, E., & Loeb, A. 2004b, *ApJ*, 617, 281
- Keshet, U., Kushnir, D., Loeb, A., & Waxman, E. 2012, *arXiv:1210.1574*
- Kitayama, T., Ito, Y., Okada, Y., et al. 2009, *ApJ*, 695, 1191
- Kubo, J. M., Stebbins, A., Annis, J., et al. 2007, *ApJ*, 671, 1466
- Kushnir, D., & Waxman, E. 2009, *JCAP*, 8, 002
- Kushnir, D., & Waxman, E. 2010, *JCAP*, 2, 025
- Laporte, C. F. P., White, S. D. M., Naab, T., & Gao, L. 2013, *MNRAS*, 435, 901
- Lau, E. T., Nagai, D., Avestruz, C. et al. 2015, *ApJ*, 806, 68
- Loeb, A., & Waxman, E. 2000, *Nature*, 405, 156
- Matsukiyo, S., Ohira, Y., Yamazaki, R., & Umeda, T. 2011, *ApJ*, 742, 47
- McDonald, M., Bayliss, M., Benson, B. A., et al. 2012, *Nature*, 488, 349
- Mantz, A. B., Abdulla, Z., Carlstrom, J. E., et al. 2014, *ApJ*, 794, 157
- Menanteau, F., Hughes, J. P., Sifón, C., et al. 2012, *ApJ*, 748, 7
- Miniati, F. 2002, *MNRAS*, 337, 199
- Miniati, F. 2003, *MNRAS*, 342, 1009
- Miniati, F. 2015, *ApJ*, 800, 60
- Montes, M., & Trujillo, I. 2014, *ApJ*, 794, 137
- Nelson, D., Genel, S., Pillepich, A., et al. 2015, *arXiv:1503.02665*
- Nishino, S., Fukazawa, Y., Hayashi, K., Nakazawa, K., & Tanaka, T. 2010, *PASJ*, 62, 9
- Ota, N., Nagayoshi, K., Pratt, G. W., et al. 2014, *A&A*, 562, A60
- Parrish, I. J., McCourt, M., Quataert, E., & Sharma, P. 2012, *MNRAS*, 419, L29
- Patej, A., & Loeb, A. 2015, *ApJL*, 798, L20
- Petrosian, V. 2001, *ApJ*, 557, 560
- Petrosian, V., Bykov, A., & Rephaeli, Y. 2008, *Sp. Sci. Rev.*, 134, 191
- Presotto, V., Girardi, M., Nonino, M., et al. 2014, *A&A*, 565, A126
- Rephaeli, Y., Nevalainen, J., Ohashi, T., & Bykov, A. M. 2008, *Sp. Sci. Rev.*, 134, 71
- Rudick, C. S., Mihos, J. C., & McBride, C. K. 2011, *ApJ*, 732, 48
- Ryu, D., Kang, H., Hallman, E., & Jones, T. W. 2003, *ApJ*, 593, 599
- Ryu, D., Kang, H., Cho, J., & Das, S. 2008, *Science*, 320, 909
- Sarazin, C. L. 1999, *ApJ*, 520, 529
- Sari, R., Piran, T., & Narayan, R. 1998, *ApJL*, 497, L17
- Schaal, K., & Springel, V. 2015, *MNRAS*, 446, 3992
- Schlickeiser, R., Sievers, A., & Thiemann, H. 1987, *A&A*, 182, 21
- Sheldon, E. S., Johnston, D. E., Masjedi, M., et al. 2009, *ApJ*, 703, 2232
- Skillman, S. W., Xu, H., Hallman, E. J., et al. 2013, *ApJ*, 765, 21
- Stanford, S. A., Brodwin, M., Gonzalez, A. H., et al. 2012, *ApJ*, 753, 164
- Takizawa, M., & Naito, T. 2000, *ApJ*, 535, 586
- Takizawa, M. 2002, *PASJ*, 54, 363
- Takizawa, M. 2008, *ApJ*, 687, 951
- Totani, T., & Kitayama, T. 2000, *ApJ*, 545, 572
- Tozzi, P., Santos, J. S., Jee, M. J., et al. 2015, *ApJ*, 799, 93
- van Dokkum, P. G., Abraham, R., & Merritt, A. 2014, *ApJL*, 782, L24
- Vazza, F., Eckert, D., Brueggen, M., & Huber, B. 2015, *arXiv:1505.02782*
- Vink, J. & Laming, J. M. 2003, *ApJ*, 584, 758
- Watson, W. A., Iliev, I. T., D'Aloisio, A., et al. 2013, *MNRAS*, 433, 1230
- Waxman, E., & Loeb, A. 2000, *ApJL*, 545, L11
- Williamson, R., Benson, B. A., High, F. W., et al. 2011, *ApJ*, 738, 139
- White, S. D. M. 1994, *arXiv:astro-ph/9410043*
- Yamada, K., & Kitayama, T. 2005, *PASJ*, 57, 611
- Zandanel, F., & Ando, S. 2014, *MNRAS*, 440, 663